doi:10.26443/seismica.v2i4.1668

Consideration of rupture kinematics increases tsunami amplitudes in far-field hazards assessments

Diego Melgar * [1,2]

[1]Department of Earth Sciences, University of Oregon, Eugene, OR, USA, [2]Cascadia Region Earthquake Science Center, Eugene, OR, USA

Author contributions: *Conceptualization*: D. Melgar. *Methodology*: D. Melgar. *Software*: D. Melgar. *Formal Analysis*: D. Melgar. *Resources*: D. Melgar. *Writing – original draft*: D. Melgar. *Visualization*: D. Melgar. *Project administration*: D. Melgar. *Funding acquisition*: D. Melgar.

Abstract Tsunami hazard assessments often assume that co-seismic crustal deformation occurs instantaneously, particularly in probabilistic tsunami hazard analyses (PTHA). However, this simplification neglects the kinematics of rupture propagation, which may influence tsunami amplitudes at distant sites. Building on previous work, this study investigates the impact of rupture kinematics – specifically rupture directivity and duration – on far-field tsunami amplitudes. Using 2600 synthetic megathrust earthquake scenarios along a 1500 km segment of the Alaskan subduction zone, I model tsunami propagation with both instantaneous and time-dependent rupture assumptions. Simulations reveal that source kinematics can significantly rotate the tsunami radiation pattern and increase peak amplitudes by over 30% at far-field sites for large (M_w>9.0) events. When incorporated into a full PTHA framework, the inclusion of rupture kinematics systematically increases hazard estimates at most coastal locations. These results suggest that neglecting rupture kinematics may lead to underestimation of far-field tsunami hazard, particularly for large, unilateral ruptures. I recommend the formal inclusion of rupture kinematics in both deterministic scenario design and probabilistic hazard frameworks to better capture the full range of potential tsunami impacts.

Production Editor:
Gareth Funning
Handling Editor:
Jonathan Weiss
Copy & Layout Editor:
Abhineet Gupta

Received:
March 25, 2025
Accepted:
November 19, 2025
Published:
January 24 2026

Non-technical summary Tsunamis are large surges of sea water most commonly caused by undersea earthquakes. To prepare for future tsunamis, scientists run computer simulations to estimate how big the waves might be and how often they could happen. These simulations are used to make maps and design buildings that can withstand tsunami impacts. Most of these models assume that when an earthquake breaks a fault that this happens all at once. But in reality, earthquakes unfold over time – sometimes taking several minutes to rupture hundreds of miles of fault. This study shows that the way an earthquake breaks a fault (called "rupture kinematics") can change the size and timing of the tsunami waves that reach faraway places, like Hawaii or the US West Coast. By modeling thousands of possible earthquakes along Alaska's subduction zone, I found that accounting for the way earthquakes move along the fault can make the tsunami waves significantly larger -— especially for very big earthquakes. In some cases, ignoring this time evolution could underestimate the impacts by 30% or more. This means current tsunami hazard assessments may be biased towards underestimation. To better prepare for future tsunamis, I recommend updating how these assessments are done to include more realistic earthquake behavior.

1 Motivation

1.1 A brief overview of tsunami hazard assessments

Tsunamis, particularly those that result from earthquakes, continue to be a major hazard source for coastal communities. Between 1998 and 2017 they were responsible for 20% of all fatalities caused by natural hazards and 10% of all associated economic losses (UNDRR, 2018). These figures are profoundly influenced by the 2004 M9.2 Sumatra, Indonesia and the 2011 M9.0 Tohoku, Japan, earthquakes (Mori et al., 2011; Titov et al., 2005) which had far-reaching impacts – these sobering numbers highlight the importance of developing quantitative methodologies for establishing the plausible tsunami intensities a particular region can expect in the future.

Assessments of tsunami hazards that attempt to quantify this typically fall into two categories: deterministic scenarios, and fully probabilistic calculations, with the choice of approach depending on the application. The use of scenarios is common in emergency planning and community organization where a fully probabilistic calculation may be considered unnecessarily complex and potentially obfuscating the purpose of the hazard assessment. In this approach a large event, sometimes dubbed the *maximum credible event* (MCE), is defined based on expert consensus, hydrodynamic modeling is carried out to establish amplitudes or inundation extents, and the results are then used to create products

*Corresponding author: dmelgarm@uoregon.edu

suitable for the chosen application. The choice of event, and with what fidelity it captures what is actually likely, has a first-order impact on the usefulness of the hazard assessment when a tsunami finally occurs.

The second and more complex approach is probabilistic tsunami hazard analysis (PTHA) – a review of the fundamentals of this framework can be found in Grezio et al. (2017). Generally, a suite of tsunami sources (earthquake or otherwise) are assumed and used as initial conditions for hydrodynamic propagation. Tsunami waves are modeled from the locations of the sources to the sites of interest. Importantly, rates of occurrence of each tsunami source or sources must be defined, and at this point, a mathematical formalism, first defined by Geist and Parsons (2006), can be used to calculate a *tsunami hazard curve* which reflects the probability of exceeding a certain tsunami amplitude over a certain period of time called the *return period*. Figure 1 depicts an example hazard curve for the town of Sitka, Alaska, obtained from the results of this work, the particulars of the computation are explained later – it shows that, if the calculation is to be believed, there is a ∼50% chance of a tsunami that exceeds (is larger) than 2 m in the next 50 years. This probability increases to ∼80% if we instead consider the next 125 years and becomes a near certainty if we consider the next 500 years. These curves codify such probabilistic statements and are very useful because they allow engineers to select specific return periods relevant to the design of different kinds of structures. The tsunami flow depths at a specific probability level and return period, as well as other useful quantities like the flow speed, can be used by engineers as the *load* that a specific structure needs to be built to withstand. In the example in Figure 1 the 50-year return period might be a useful guide for design of single-family homes or residential apartments whose useful life might not be expected to exceed too much longer than that. However, for designing critical infrastructure a longer return period such as 500 years might be more suitable, and even, perhaps, not long enough.

PTHA has found significant success, and numerous research articles as well as technical documents from operational agencies exist which detail how the framework can be applied to specific contexts. These regions include Australia (Davies and Griffin, 2018), Chile (González et al., 2019), Indonesia (Horspool et al., 2014), the Mediterranean (Sørensen et al., 2012), Mexico (Salazar-Monroy et al., 2021), the South China Sea (Li et al., 2016; Sepúlveda et al., 2019), and the United States (University of Washington Working Group, 2017), just to name a few. Of note is that, when a probabilistic calculation for the tsunami hazard is made, we typically distinguish between *near-field* sources, which can be *local* if they are within 100 km of a site, or regional if between 100–1000 km, and *far-field* sources which are further afield, usually more than 1000 km away (Hirshorn et al., 2020). In this paper I focus on the dominant source of hazard which are earthquake induced tsunamis and zero in on a potential characteristic of them that can affect a PTHA calculation: the details of the time-evolution – the kinematics – of the rupture process.

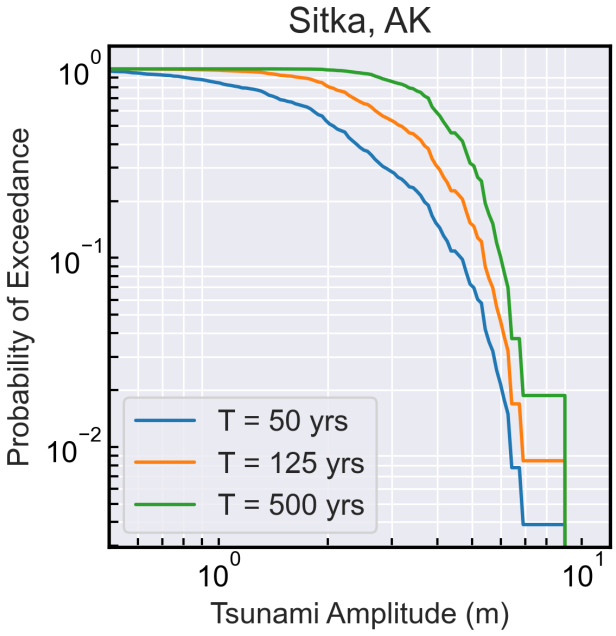

Figure 1 Example tsunami hazard curves for Sitka, Alaska. Shown are curves for 3 return periods: 50, 125, and 500 years.

1.2 Rupture complexity: kinematics and tsunamigenesis

There are numerous complexities associated with the rupture process which may contribute to the particularities of tsunamigenesis and have been the subject of scrutiny in the literature before.

The most important one is perhaps the heterogeneity of slip. Out of a desire to minimize uncertainty and due to the fact that future slip distributions of large events are, at present, impossible to forecast, tsunami hazard assessments have relied on homogeneous or very simplified slip distributions (González et al., 2009; Witter et al., 2011). More recently, there has been a concerted effort to use more realistic heterogeneous slip distributions (Geist and Lynett, 2014; Davies et al., 2015; Mori et al., 2017) and in fact, Melgar et al. (2019) noted, through numerical experimentation, that, all things being equal (fault length and width, depth, and magnitude) heterogeneous slip leads to consistently larger tsunami amplitudes in the near-field of an earthquake compared to homogeneous or quasi-homogeneous slip. The issue has been discussed for far-field modeling as well (Davies and Griffin, 2018) with the same conclusion being reached – that simplified slip distributions bias tsunami calculations towards the low end of the spectrum. A modern tsunami hazard assessment must consider realistic slip heterogeneity.

In these previous works, and many others, the issue of the time evolution of slip, the rupture kinematics, has received some cursory attention. Typical rupture speeds for most tsunamigenic earthquakes are ∼2.5–3.5 km/s (Melgar and Hayes, 2017), meanwhile tsunami propagation speeds in water depths of 100–1000 m, typical of continental shelves, are a much slower 0.03–0.1 km/s. From this rudimentary calcula-

tion alone, one would expect the kinematics of rupture to have no measurable influence on the ensuing tsunami. The rupture propagates so fast, from the point of view of the tsunami waves, that it is essentially instantaneous.

Because of this, it is common in tsunami modeling to assume that the deformation associated with an earthquake that sets up the tsunami initial condition occurs instantaneously (Grezio et al., 2017). This is attractive because it can speed up computation – capturing the full details of time-evolving crustal deformation and its coupled relationship to tsunamigenesis requires taking modeling time steps during the rupture process that are much shorter than what is required if instantaneous deformation can be assumed. Indeed, a numerical study by Williamson et al. (2019) found that for earthquakes M7.5–M9.0 in the near field there is less than a 1% difference in tsunami amplitudes resulting from considering instantaneous vs. time-dependent crustal deformation associated with the earthquake. Meanwhile Sementsov et al. (2024) found by numerical analysis of 16 large events (1992–2021), that at distances of a few source lengths from the event, 10 of the 16 earthquakes showed greater tsunami energy for kinematic than for static sources (up to ∼9%).

Two important corollaries to the above results are worth mentioning. First, when ruptures are very slow, close to the propagation speeds of tsunamis in continental shelves, then the effects can be significant and might lead to larger tsunamis than when considering instantaneous rupture (Riquelme et al., 2020; Riquelme and Fuentes, 2021). However, slow earthquakes like this are very rare, and restricted to the special class labeled "tsunami earthquakes" which rupture the shallow-most part of a subduction zone and create tsunamis that are much larger than expected for their magnitude while also radiating very weak seismic energy (Kanamori, 1972; Newman and Okal, 1998; Hill et al., 2012; Sahakian et al., 2019). The second instance where rupture speed can play a significant role was identified by Williamson et al. (2019), and it has to do with far-field tsunamis. There, modeling showed that while the impacts in the near-field were negligible, in the far-field there was enough time, given the long propagation distances, for the differences to amount to meaningful variations in amplitude. This was especially true for long, high magnitude, unilateral ruptures where the source process can take many minutes. That study simply mentioned this potential difference without analyzing it in detail as their focus was the near-field hazard. However, there exists some limited evidence that rupture kinematics, in fact, need to be considered in the far-field. Modeling open-ocean observations from the TOPEX/Poseidon satellite altimeter that measured the tsunami waves in the deep Indian Ocean from the extremely long rupture (∼1600 km, ∼10 min) associated with the 2004 M9.2 Sumatra earthquake appears to indeed require consideration of the time evolution of rupture (Fujii and Satake, 2007; Suppasri et al., 2010).

1.3 Hypothesis tested in this work

Given the context discussed above, in this work I expand on the findings of Williamson et al. (2019) and use numerical models to explore the impacts of rupture kinematics in *far-field* tsunamis. Specifically, I test the hypothesis that rupture can be safely assumed to be instantaneous. I will conclude that it cannot, especially for large (M8.5+) and very large (M9.0+) events, and that ignoring rupture kinematics can have a measurable impact in estimated far-field tsunami amplitudes. Finally, I discuss potential approaches for formally including rupture kinematics in hazard assessments.

2 Methods

In order to focus specifically on the issue of rupture kinematics, and because they were studying primarily near-field effects, Williamson et al. (2019) created a sandbox subduction zone with simplified bathymetry and with infinite length along-strike. That approach was valuable, it allowed the authors to untangle confounding variables such as the complexity introduced by bathymetry. Here, I focus on far-field effects where it is harder to create a useful simplified spherical model of the world's oceans. Instead, I selected a ∼1500 km segment of the Alaskan subduction zone (ASZ, Figure 2) as the source region. I place different homogeneous sources there and propagate the tsunamis to far-field virtual tide gauges to study the impacts of different source kinematics.

2.1 The earthquake sources assumed and their kinematics

As noted previously, slip heterogeneity can have significant impacts on the details of a tsunami. Here however, to focus on the contributions of kinematics, I rely primarily on homogeneous slip. In the discussion I will touch on the added contributions of heterogeneous slip with a single example.

I chose the segment of the ASZ shown in Figure 2B primarily because it is large enough to fit earthquakes as large as the 1964 M9.2 event (Ichinose et al., 2007) and can thus be assumed to reasonably represent a source region capable of hosting hazardous events across a broad range of magnitudes. I then created homogeneous slip sources spanning the magnitude range M7–M9.5 using 0.1 magnitude unit bins and 100 events per bin for a total of 2600 ruptures. Because it is well established that for a given magnitude, earthquakes can have different dimensions (Blaser et al., 2010; Allen and Hayes, 2017) the ruptures are allowed to vary in their length and width. For each earthquake I make a random draw from the probabilistic length and width scaling laws for thrust earthquakes from Blaser et al. (2010). I then select a random segment of the megathrust region in Figure 2B and then compute how much homogeneous slip is necessary to reach the target magnitude. For the fault geometry I use the 3D slab model of Hayes et al. (2018), discretize it into triangular subfaults, and allow slip from the trench to a maximum seismogenic depth of 60 km which is consistent with the 1964 M9.2

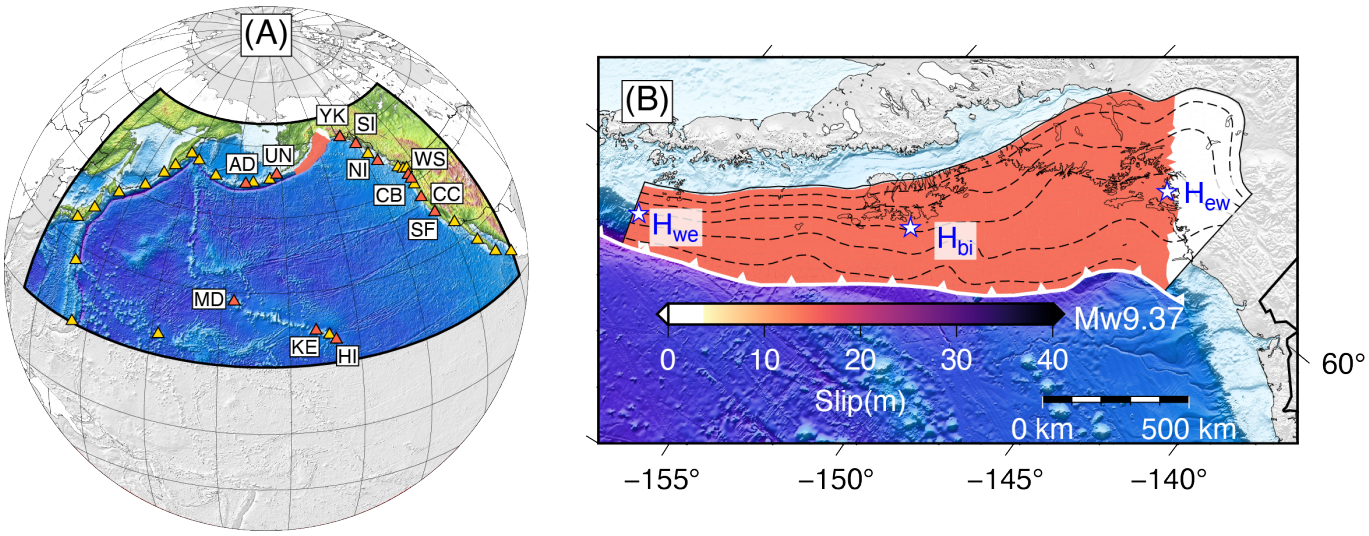

Figure 2 (A) Domain used for hydrodynamic propagation modeling. The portion of the Alaskan subduction zone assumed as the source region is shown in pink. Yellow triangles are the virtual tide gauge stations used to collect model output. Pink triangles are also virtual tide gauges, but represent sites mentioned explicitly elsewhere in the article. They are AD-Adak, UN-Unalaska, YK-Yakutat, SI-Sitka, NI-Ninstints, WS-Westport, CB-Cannon beach, CC-Crescent City, SF-San Francisco, HI-Hilo, KE-Kealia, and MD-Midway. (B) Close-up of the approximately 1500 km long stretch of the Alaskan subduction zone used as a source region in this study. Shown is a homogeneous slip M9.37 earthquake. Slab geometry is from Slab 2.0 (Hayes et al., 2018) and contoured every 10 km in depth. Three possible hypocenters to nucleate rupture are shown, H_{we} for unilateral west to east rupture, H_{bi} for bilateral rupture, and H_{ew} for unilateral east to west rupture.

earthquake (Ichinose et al., 2007) and also with the more modestly sized and more recent 2020 M7.8 and 2021 M8.2 Simeonof and Chignik earthquakes (Crowell and Melgar, 2020; Ye et al., 2022). A summary of the rupture dimensions is shown in Figure 3 and an example of a homogeneous slip source that results from this process is shown in Figure 2B. Finally for the Earth structure I assume a homogeneous half-space with rigidity of 30 GPa.

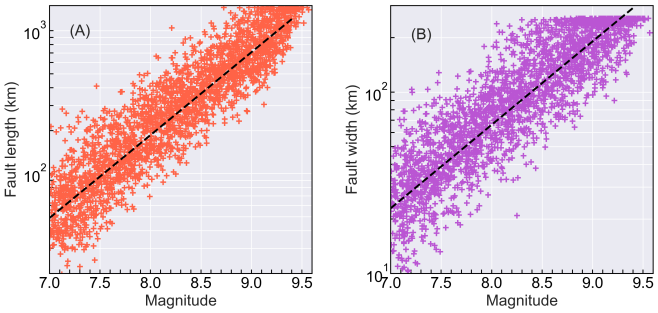

Figure 3 (A) Rupture length vs. magnitude scaling. The symbols are the length of each rupture and the dashed line is the median expected length from Blaser et al. (2010) (B) Rupture width vs. magnitude scaling. The symbols are the length of each rupture and the dashed line is the median expected length from Blaser et al. (2010)

In terms of kinematics I assume a standard uniform rupture speed of 3.0 km/s consistent with worldwide observations of megathrust ruptures (Melgar and Hayes, 2017). For each rupture a hypocenter is chosen at random from all the subfaults that participate in a particular event and the inter-fault distance is calculated based on a cubic spline interpolation on the assumed 3D fault surface. The "onset time", which is the time after the event origin at which the rupture from the hypocenter reaches a sub-fault is then simply the inter-fault distance divided by the assumed rupture speed. An example of the impact this can have on rupture duration is shown in Figure 4 where I have forced the hypocenter to be at either edge of an almost full margin M9.3 earthquake representing purely unilateral rupture. Shown as well is an event where rupture initiates in the middle for a purely bilateral earthquake. In the full-suite of events shown in Figure 3 because the hypocenter is assigned at random there is a mix of kinematic behaviors between these two extremes.

2.2 Hydrodynamic modeling

I employed the GeoClaw modeling framework (Berger et al., 2011), an open-source module within the Conservation Laws Package (Clawpack) suite (Mandli et al., 2016; Clawpack Development Team, 2024), to simulate tsunami generation and propagation. The tsunami initial condition is the seafloor deformation produced by each earthquake. For both instantaneous or static, and kinematic ruptures I calculate the crustal deformation using the triangular subfault approximation to the analytical solutions of Okada (1985, 1992) as implemented in GeoClaw. I then compute the total vertical deformation as the sum of the true vertical coseismic deformation and the "pseudo vertical" deformation introduced by horizontal advection of topography. This extra source term was first noted by Tanioka and Satake (1996) and I follow the implementation of Melgar and Bock (2015). The code then solves the two-dimensional depth-averaged shallow water equations using high-resolution finite volume methods, making it well-suited for capturing the nonlinear dynamics of tsunami waves

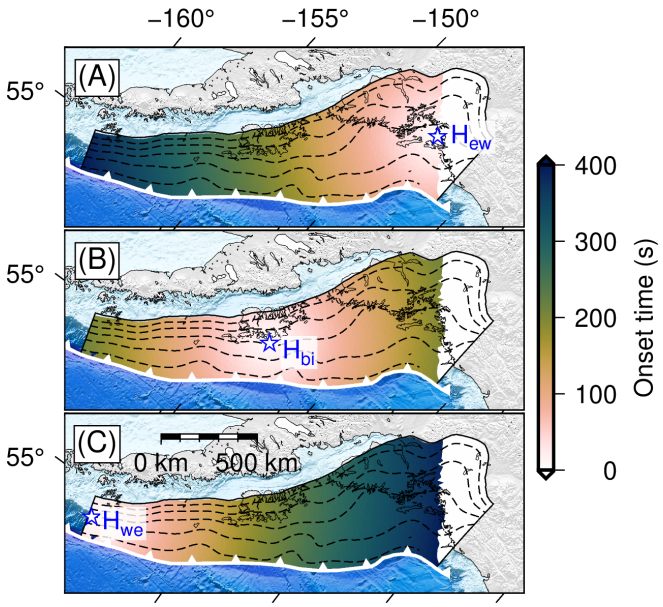

Figure 4 (A) Rupture onset times for a unilateral east-west propagating homogeneous slip M9.3 rupture. (B) Same as in (A) but for a bilaterally propagating rupture. (C) Same as in (A) but for a unilateral west-east propagating rupture.

and their interaction with complex coastal topography. To ensure numerical stability and accuracy, I set the Courant-Friedrichs-Lewy (CFL) condition to 0.75, limiting the time step size relative to the spatial grid size and wave speed. GeoClaw can handle wetting and drying processes, allowing for accurate simulation of onshore wave run-up and inundation. Tsunami waves are propagated over variable bathymetry and topography, I used the ETOPO2 2 arcmin bathyemtry dataset (NOAA National Geophysical Data Center, 2006) in deep water and the 30 arcec SRTM30+ dataset in coastal regions (Becker et al., 2009). GeoClaw incorporates adaptive mesh refinement (AMR), which dynamically increases computational resolution in regions of interest such as along inundation zones; details of the implementation are in LeVeque et al. (2011). Near the tsunami source I force the highest level of refinement to be employed for at least the duration of the rupture. Three AMR levels are used, the coarsest grid has 10 arcmin resolution, the intermediate grid 2 arcmin to match the ETOPO2 data, and the finest grid 30 arcsec to match SRTM30+. The model domain (Figure 2) covers 145° in longitude from 120° to 265°, and 60° in latitude from 10°N to 70°N. For every model, output is collected at "virtual" tide gauges (locations are in Figure 2), each gauge is placed one pixel offshore (in the AMR level 3 bathymetry) and its amplitude corrected in post-processing using Green's law to a common depth of 5 m. Each tsunami model was run for a propagation time of 14 hours. Computation wall-times vary greatly from ∼1–2 min for smaller sources to ∼10–15 min for the largest ones. Each run uses 30 CPU cores and the entire event set was run on a 128 core server allowing for 4 runs to be computed simultaneously. GeoClaw has been rigorously validated against laboratory experiments and historical tsunami events, ensuring its reliability for hazard assessment and risk analysis (González et al., 2011; Arcos and LeVeque, 2014).

3 Results and Discussion

3.1 Slip kinematics rotate the far-field tsunami radiation pattern

The most immediate result from the hydrodynamic modeling is to confirm what Williamson et al. (2019) had already identified – rupture directivity rotates the tsunami radiation pattern. In Figure 5, I show the maximum tsunami amplitude from assuming an instantaneous rupture, a bilateral one, an east to west one, and another west to east rupture for the same M9.3 homogeneous slip distribution shown in Figures 2B and 4. To first order, what can be seen is that the tsunami increases in amplitude in the direction of rupture, for example, for the East to West rupture, the tsunami is larger in Hawaii which is due West of the the subduction zone, and smaller when the rupture is West to East. For a bilateral rupture the pattern is a combination of these effects. This a purely geometric effect – the total tsunami potential energy available for wave propagation is controlled by the final coseismic deformation (Nosov et al., 2013; Melgar et al., 2019), and is the same in both instantaneous and kinematic cases.

Nevertheless, the impact of this can be significant. Figure 6 shows the differences at Hilo, Hawaii, of the tsunami when rupture is assumed instantaneous vs. when it has unilateral directivity. When rupture is "towards" Hilo (east to west), the tsunami is about 1 m larger by peak amplitude for the first 4 arriving waves. Likewise when the rupture is "away" from Hilo in the west to east direction the tsunami is slightly smaller than in the instantaneous case but also decays much faster. Interestingly the coda of the tsunami (after about 3 hours) has very similar amplitudes in all cases.

Figure 7 shows the effect at other sites across the basin. For each one, I selected a kinematic rupture that shows some amplitude difference with respect to the instantaneous rupture assumption; sometimes that is the east to west, others the west to east. I highlight, however, that tsunami propagation is non-linear and bathymetry is complex so the effect isn't that simple or easy to anticipate before the modeling is run. Depending on the complex interplay between those two factors, for any given rupture, the resulting tsunami can be smaller or larger at a specific site. This is shown in Figure 8 where I plot the relative and absolute differences in maximum amplitudes between the instantaneous and different kinematic ruptures at a variety of coastal sites. Overall there is a trend where if rupture is towards a site the amplitude is larger than if it is away from it. The bilateral rupture is a complex combination of both, and there are numerous sites for which the plotted event are exceptions to this trend.

Evidently the effect is a strong function of source duration which itself is a function of magnitude – larger events rupture longer faults and have longer source processes with more time for the kinematic effect to be manifest. Figure 9 shows an example of this. Here, I have plotted the differences between instantaneous

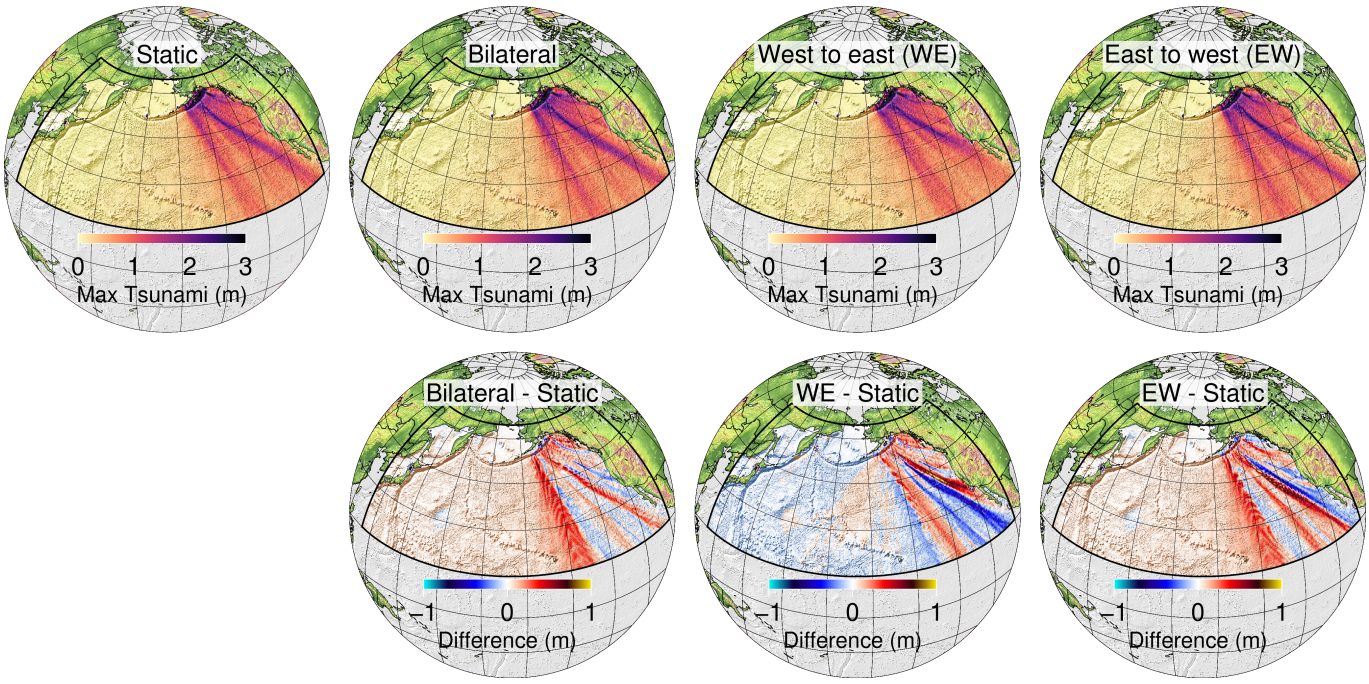

Figure 5 Maximum tsunami amplitudes resulting from assuming an instantaneous (static) rupture vs. unilateral east to west, west to east, or bilateral ruptures shown in Figure 4. Differences between each of these time-dependent kinematic ruptures and the static one are shown below each.

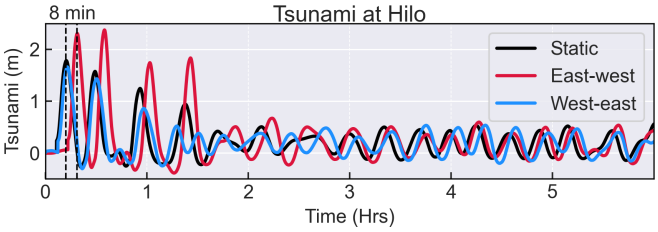

Figure 6 Tsunami amplitude at Hilo, Hawaii from instantaneous (static) rupture of the earthquake shown in Figure 2 and from time-dependent rupture with east to west or west to east directivity. Note the 8 min arrival time difference for the peak amplitude.

and kinematic ruptures for events with M7.8, M8.3, and M8.8, and compared and contrasted with the effect for an M9.3 rupture in Figure 8. The differences are more and more significant with increasing magnitude, they are smaller than 5% for the M7.8 event and as large as 30% for the M9.3 event. Now, while these changes are most important for the largest events, even for more "modest" ruptures like the M8.3 shown in Figure 9 the differences can be as high as ∼10–15 % suggesting that, when considering ensembles of ruptures, such as in PTHA, the effect might have a measurable impact in the resulting hazard calculation, and this will be discussed at length soon.

3.2 Implications for single event hazards assessments

The purpose of selecting a Maximum Credible Event (MCE), whether for far- or near-field sources, is to have a single scenario from which products such as inundation maps or evacuation times can be produced, and which reflects a credible worst case. The goal is to avoid the complexities and potential confusion of a full probabilistic calculation while at the same time producing information that reflects what is possible and is actionable and useful.

As an example of this, for both Hawaii and the western states of Washington, Oregon, and California, events in Alaska are considered the dominant source of far-field hazard. To model them, simple quasi-homogeneous slip single scenarios are routinely used for hydrodynamic calculations and hazards product generation (González et al., 2009; Priest et al., 2013; Butler et al., 2016). Figure 10 reflects the potential impacts of considering more realistic sources. I produced a stochastic heterogeneous M9.3 slip model (Figure 10A) covering the exact same extent as the homogeneous slip model in Figures 2B and 4, and calculated the resulting tsunami, both when assuming an instantaneous rupture process, and when assuming a completely unilateral east to west rupture. The tsunami time series at the same locations as in Figure 8 are shown in Figure 10B. The differences can be significant when moving from a homogeneous instantaneous rupture to a heterogeneous instantaneous rupture. At Hilo, HI, where we already knew the effect would be important, the peak amplitudes increase by 39% between the homogeneous static and heterogeneous static sources and by 86% between the homogeneous static and heterogeneous kinematic sources. At other US West Coast sites like Westport, WA, Cannon Beach, OR and San Francisco, CA, the effect is more modest, closer to a ∼10–20 % increase. Notably, considering a kinematic heterogeneous slip rupture increases the amplitudes, not just of the first arrivals, but frequently of the entire wavetrain.

Overall, what can be observed in Figure 10 is that al-

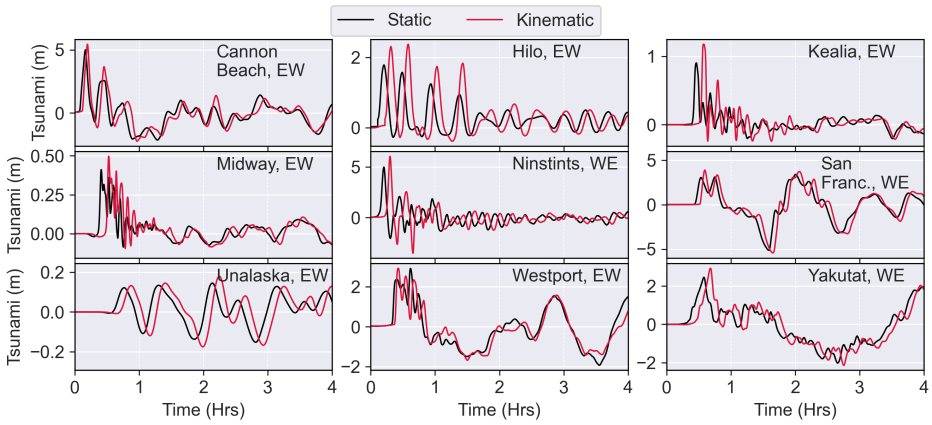

Figure 7 Comparison of tsunami amplitude at selected sites between instantaneous or static rupture and unilateral "kinematic" rupture. For some of the sites the maximum difference is with the east to west (EW) rupture, for others with the west to east (WE) rupture.

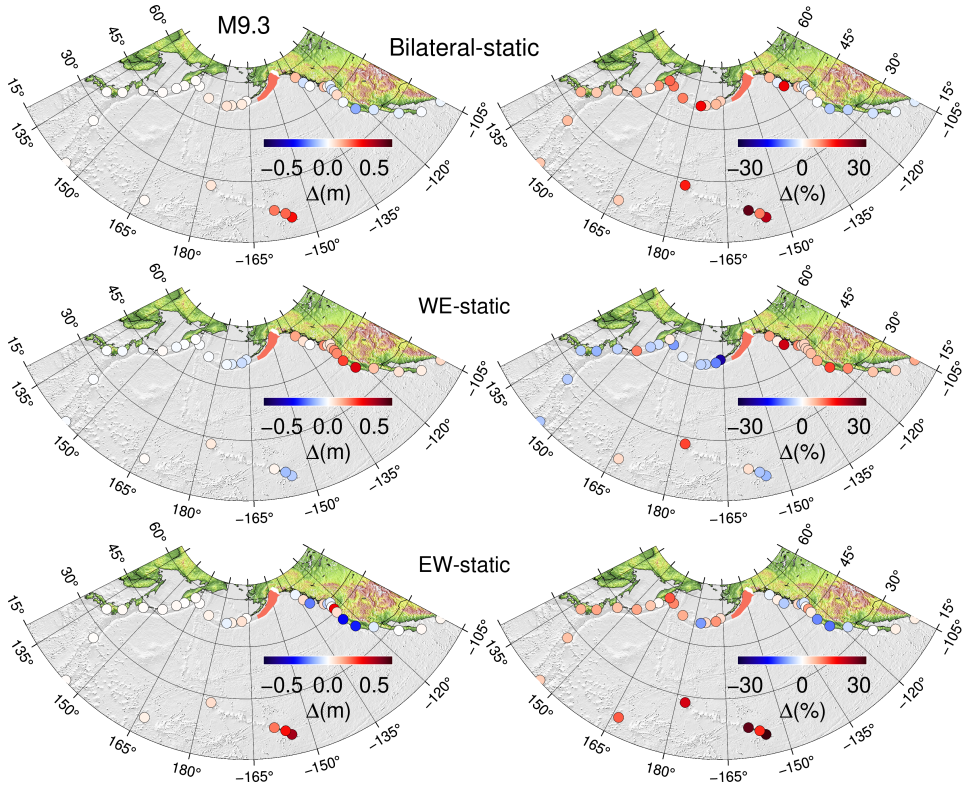

Figure 8 Differences in the maximum recorded amplitudes at coastal sites between instantaneous (static) rupture, and bilateral, east to west (EW), or west to east (WE) ruptures. The differences are shown as absolutes values (left column) and relative percentages (right column). In each, the part of the fault assumed to have ruptured is shown in pink.

lowing for more realistic heterogeneous slip has a major impact. This has been clearly articulated already in several previous works (Geist, 2002; Goda et al., 2014; Davies and Griffin, 2018; Melgar et al., 2019), but compounding that increase, the source kinematics could potentially make an already impactful event significantly worse. The conclusion here is that modelers and hazards practitioners, when ideating MCEs, should consider potential tsunami directivity from source kinematics.

3.3 Consideration of kinematics can increase hazard in far-field PTHA calculations

Figures 8–10 tell a compelling narrative that the source kinematics can matter in the far-field and can frequently make peak amplitudes appreciably higher. But they also show that kinematics can *sometimes* make the amplitudes smaller. So, for applications such as PTHA, where we consider ensembles of ruptures, an obvious question is whether source kinematics increase, decrease, or leave the overall hazard unchanged when compared to the instantaneous rupture assumption. This will ultimately dictate how modelers should consider this increased source complexity in formal PTHA

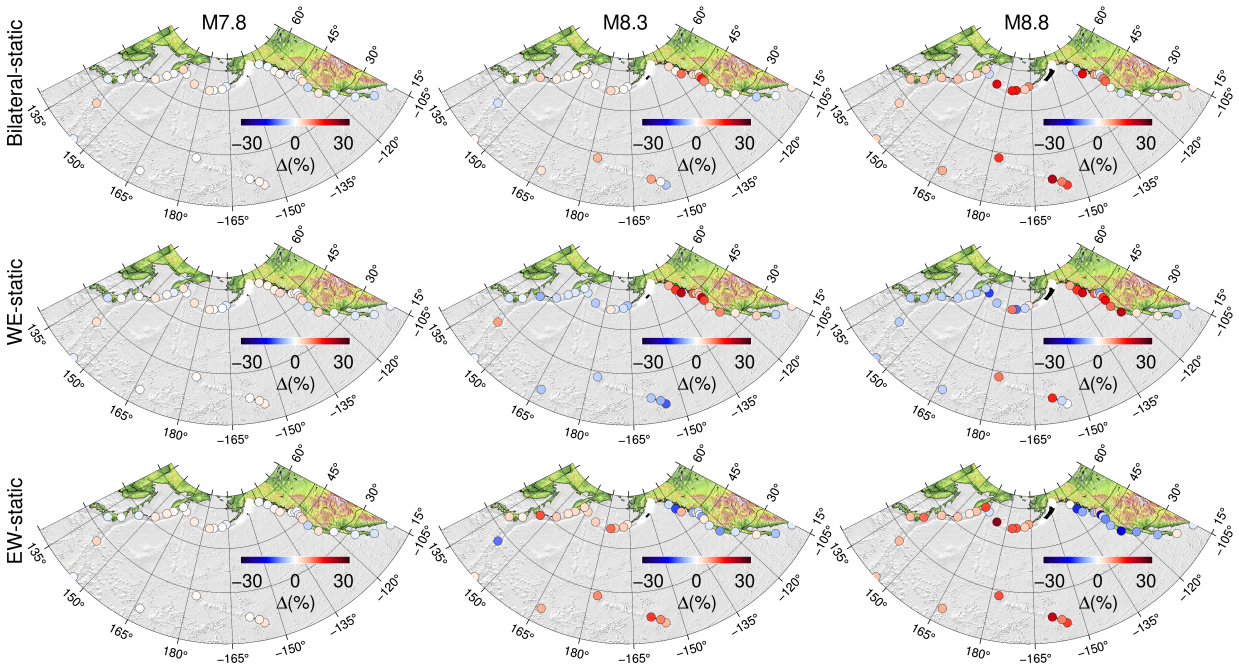

Figure 9 Differences in the maximum relative recorded amplitudes at coastal sites between instantaneous (static) rupture, and bilateral, east to west (EW), or west to east (WE) ruptures for homogeneous slip models with M7.8, M8.3 and M8.8. The part of the fault assumed to have ruptured is in blue.

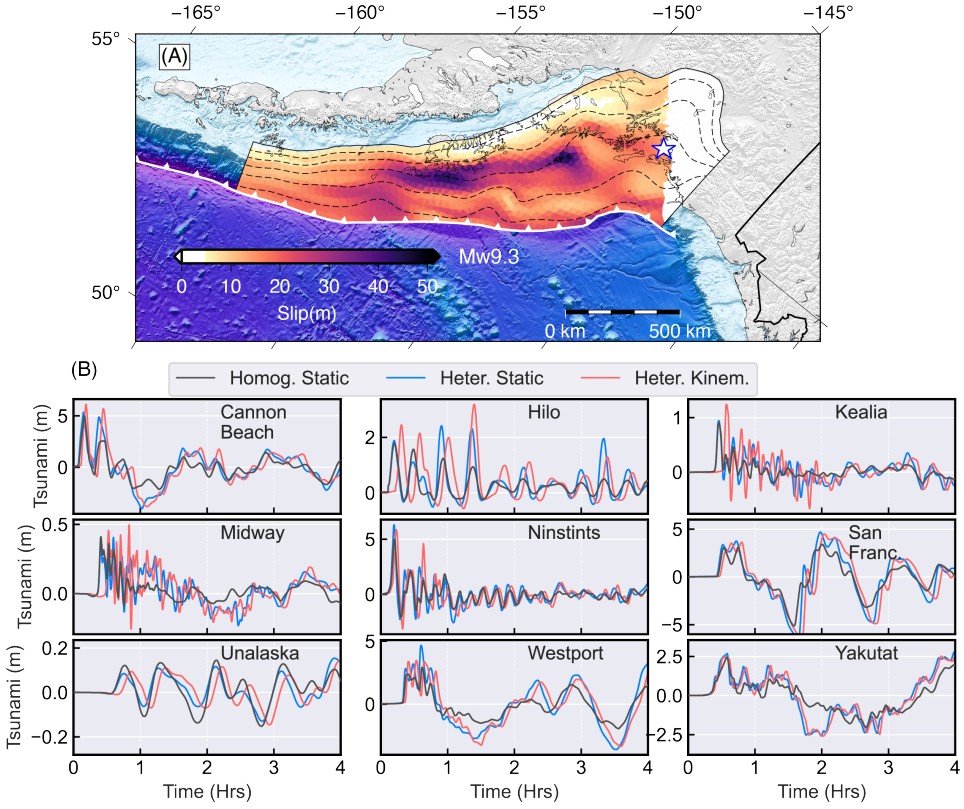

Figure 10 Effect of slip kinematics on single scenario tsunami hazard estimates. (A) Heterogeneous stochastic slip M9.3 covering the same rupture as the event in Figures 2 and 4. The blue star is the hypocenter. (B) Resulting tsunamis at locations highlighted in Figure 2.

calculations.

Figure 11A shows a summary of the differences for all 2600 ruptures at four selected sites which are representative of the overall behaviors seen across the basin. At three of them (Adak, Midway, and Hilo) the effect is to increase the overall hazard – this is more clearly visible as the magnitude increases. This can also be readily seen in Figure 11B as a function of the distance between the centroid and the hypocenter, which is a proxy of how unilateral a rupture is. The effect is noticeable for distances as short as 90–150 km and is extremely prominent for longer distances. For one of the sites (Cres-

cent City), the effect is sometimes to increase the amplitude, both as a function of magnitude and centroid–hypocenter distance, but other times the amplitude is decreased. At that site in particular we see that the median differences are negative – kinematics reduce the overall hazard.

What is the impact of this on a fully probabilistic hazard calculation? For each coastal site I calculated the hazard curves using the PTHA formulation described in Melgar et al. (2019). For the magnitude frequency distributions (MFDs) I assumed a linear Gutenberg-Richter-like distribution, and a tapered one that has decreasing rates for all events with M_w>8.3. The distributions are shown in Figure 12 and both are taken from the US National Seismic Hazard Map for Alaska as described by Powers et al. (2024). The resulting hazard curves for the same four sites as Figure 11 are shown in Figure 13. For the same three sites where we saw significant amplitude increases (Adak, Midway, and Hilo) when considering kinematic ruptures, we see significant increases in the resulting hazard curves. Because the amplitude differences are greatest at larger magnitudes and these events have lower rates of occurrence, I had hypothesized that this effect would be much more pronounced at long return intervals such as $T = 500\,\mathrm{yr}$. However, the increase in hazard is evident for the much shorter return period of $T = 50\,\mathrm{yr}$ as well. This is most likely a result of the fact that the increase to hazard due to source kinematics is non-negligible for events with "modest" magnitudes as well as for those with relatively short centroid–hypocenter distances (Figure 11).

For Crescent City, where the kinematic ruptures frequently produced smaller amplitudes than the static ones (Figure 11) I do indeed find a very slight reduction in hazard when considering the kinematic source process. As interesting as this behavior is, it is not the norm – only at five of the coastal sites is there a slight reduction in hazard while at the rest, the hazard increases when considering kinematic ruptures.

I note that another important factor to consider is the overall impact that kinematic ruptures might have on the resulting hazard curves when considering different MFDs. The tapered distribution shown in Figure 12 has a much lower yearly rate of occurrence for large events. A priori, one might think this would make the effect of considering kinematic sources less significant because those events where the difference is largest receive a smaller weight in the calculation. However, in Figure 14, I show the hazard curves for the tapered distribution compared to the log-linear Gutenberg-Richter distribution and find that this is not the case. Overall, the tapered MFD leads to a substantially lower hazard compared to the linear MFD, because large events are occurring less frequently, but for any given MFD, the difference between static and kinematic sources remains. This suggests strongly that even with an MFD that reduces the frequency of large events, considering kinematics remains important.

Ultimately the importance of this effect will become clearer as more events are modeled and observed carefully. Sementsov et al. (2024) already found, from a retrospective analysis of large events, that there is a modest increase in amplitude when considering rupture kinematics. New open ocean observations for large events, such as those from satellite altimetry, for example for the recent 400 km long M8.8 Kamchatka earthquake (Ruiz-Angulo et al., 2025), or from fiber optics (Taha et al., 2025) will help to prove (or disprove) the modeling results in this work.

3.4 Limitations of the approach, other confounding variables, and open questions

Finally, I note a few limitations of the approach and confounding variables that can affect my interpretation of the impact of source kinematics on far-field tsunami hazard assessments.

The computed sources do not consider depth-varying rigidity (Bilek and Lay, 1999). This is an important extra variable that can contribute to increased complexity in tsunamigenesis. If slip extends to shallow low-rigidity materials, coseismic deformation can increase significantly with the attending increase in the resulting tsunami amplitudes (Saito and Furumura, 2009). In these materials, rupture slows down even more (Riquelme and Fuentes, 2021) approaching tsunami propagation speeds making the kinematic effect even more pronounced. Further, higher-order mechanics such as plasticity can augment vertical coseismic deformation by an additional, non-negligible amount (Wilson and Ma, 2021). Full consideration of these complexities is becoming increasingly necessary.

The hydrodynamic code I used does not account for dispersion. Studies have shown that, particularly in the far-field, dispersion can significantly alter arrival times and, due to non-linear propagation, the way that different phases of the tsunami wavetrain interact with each other (Glimsdal et al., 2013; Grilli et al., 2012; Baba et al., 2017). This means that, if modeling of time series at trans-oceanic distances requires very accurate interactions between phases, then dispersion cannot be ignored. However in those previous works, significant impacts to peak amplitudes have not been observed. So, while dispersion would likely change some of the details of the shapes of the time series seen in Figures 6, 7, and 10, I would not expect the general finding that source kinematics have a meaningful impact on far-field tsunami hazards, to change. Nonetheless, I recognize that an accurate PTHA calculation that seeks to be useful for decision-making products ought to account for this added complexity.

Bathymetry remains an important confounding variable and one whose impact is difficult to ascertain before the modeling is carried out. Due to the complexity introduced by non-linear tsunami wave propagation, it is possible for sites close to each other to be affected by the increased hazard introduced by kinematic sources to different degrees (e.g., Figures 8 and 9); so much so that, even if for the most part we expect hazard will increase, some sites (such as Crescent City in this work) might see a slight reduction in hazard.

Of course, whatever the impact, the hazard curves in Figures 13 and 14 suggest that it is a significant effect

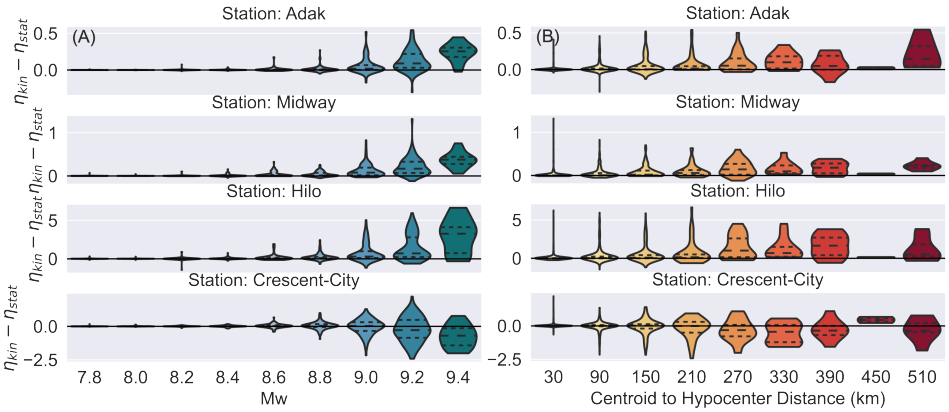

Figure 11 Differences between peak tsunami amplitude from kinematic sources (η_{kin}), and from static or instantaneous rupture (η_{stat}) for all events at four selected sites – (A) results disaggregated into magnitude bins, and (B) into distance between the rupture centroid and the hypocenter. For each violin the median and quartiles are shown in dashed lines.

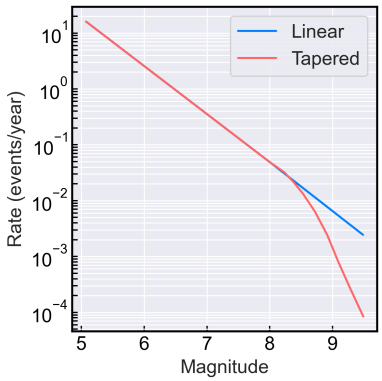

Figure 12 Magnitude frequency distributions assumed for hazard curve calculations taken from Powers et al. (2024). The "linear" MFD assumes a constant b-value as would be expected from Gutenberg-Richter (G-R) statistics. The "tapered" distribution assumes that after M8.3, events are less frequent than what is predicted by G-R statistics, and this is justified by the historical catalog of events in Alaska.

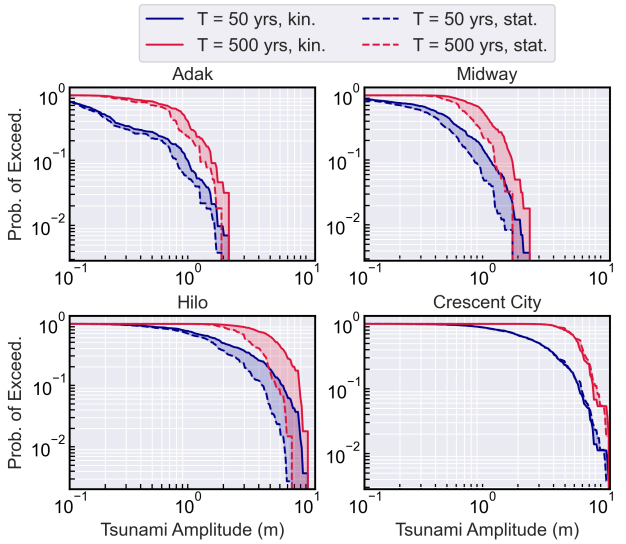

Figure 13 Hazard curves at two return periods ($T = 50\,\mathrm{yr}, 500\,\mathrm{yr}$) for the same four coastal sites as Figure 11. The curves assuming instantaneous sources are shown in dashed lines and the ones for kinematic ruptures are in solid lines. The differences between them are shaded for clarity.

and it ought to be considered. I note however, that the overall change to a specific site's hazard will be the sum of the far-field hazard contributions of many subduction zones, not just one, in addition to the contributions from any local sources. I stress that the findings here suggest that the tsunami hazard to, for example, Hilo is higher for events from Alaska, but it is not easy to see without further modeling whether this will be equally true for all far-field sources that affect that site and whether in aggregate this will lead to an overall more dangerous hazard curve. At most what I can say is that there is a significant chance that the present methodology used to infer far-field hazards is most likely systematically biased towards underestimating them, but quantifying to what extent this bias exists requires a significant amount of new numerical modeling.

Furthermore, the results shown here only account for impacts to coastal amplitudes and say nothing of how this potential increase in hazard will change inundation estimates. It is ultimately this inland extent and intensity of flooding that is of use for many applications such as evacuation maps. Because the increases in amplitudes extend to more than just the first or largest arriving wave (e.g., Figure 7) it is reasonable to expect that the impact will be non-negligible. I admit however, that this is speculation and highlight again that it is not easy to foretell the extent of the effect without new numerical modeling.

More practically, I would recommend conceptualizing the issues using something like the operational distance bands used in tsunami warning as a practical scaffold for when rupture kinematics are most consequential (Hirshorn et al., 2020), local ($\leq$100 km), regional ($\leq$1000 km), and teletsunami (>1000 km), because far-field (teletsunami) amplitudes are where rupture duration and directivity most strongly reshape the long-period tsunami spectrum. In particular for tsunami warning, as rapid, more accurate forecasts become desirable, it will be important to consider the effect at teletsunami distances.

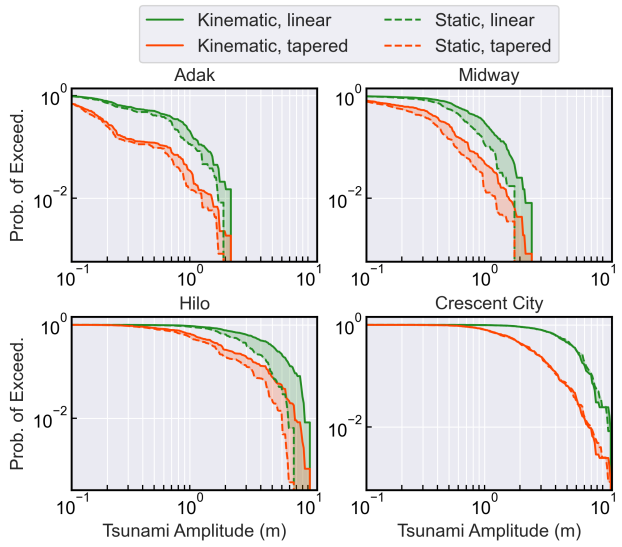

Figure 14 Hazard curves at a return period of $T = 125$ yr assuming the two magnitude frequency distributions (linear and tapered) from Figure 12 and the impact between static and kinematic ruptures. The differences between them are shaded for clarity.

I note in closing, that accounting for source kinematics slows down computation time – kinematic runs, depending on magnitude, are as much as 30% slower by CPU wall time. I argue here that this increased computational load is, in the face of the findings in this paper, an insufficient argument to justify ignoring an important effect. If computational cost is not a constraint, include kinematics universally across all magnitude ranges. Nonetheless, if resources are constrained, prioritize kinematics for great earthquakes ($M_w \gtrsim 8.5$) and for sites in the teletsunami band. A modern far-field tsunami hazard assessment must account for source kinematics to some degree.

4 Conclusions

This study demonstrates that the commonly held assumption of instantaneous earthquake rupture in far-field tsunami modeling is not always valid. Using thousands of synthetic earthquake scenarios along the Alaskan subduction zone, I show that rupture kinematics – particularly rupture direction and duration – can significantly alter the amplitude and arrival time of tsunami waves at distant coastlines.

Key findings include:

- Rupture directivity rotates the tsunami radiation pattern, increasing amplitudes in the direction of rupture and decreasing them in the opposite direction. This effect is amplified for larger earthquakes with longer rupture durations.

- Far-field sites, such as those in Hawaii and along the US West Coast, can experience meaningful increases in tsunami amplitude – often exceeding 30% – when rupture kinematics are considered.

- Probabilistic tsunami hazard analysis (PTHA) incorporating rupture kinematics shows a consistent increase in hazard at most coastal sites, particularly for longer return periods and larger magnitudes. In rare cases, hazard can be slightly reduced, but this is the exception rather than the rule.

- The inclusion of rupture kinematics in deterministic scenario modeling (e.g., maximum credible events) can result in significantly different and potentially more realistic hazard assessments compared to traditional static assumptions.

These results imply that current far-field tsunami hazard assessments, which largely neglect source kinematics, are likely biased toward underestimating tsunami amplitudes. A general recommendation is that future PTHA frameworks and deterministic scenario development formally incorporate rupture kinematics to better reflect the physical processes that govern tsunamigenesis and to improve the reliability of hazard products used in coastal planning and infrastructure design.

Acknowledgements

I extend my gratitude to Ignacio Sepulveda for ongoing discussions of all things tsunami. I thank the Associate Editor Jonathan Weiss and three anonymous reviewers for constructive feedback. This research was supported by the Cascadia Region Earthquake Science Center (CRESCENT). CRESCENT is funded by the National Science Foundation Cooperative Agreement #2225286. Additional funding is provided by the United States Geological Survey Cooperative Agreement #G25AC00531 and Pacific Gas and Electric Company. Any opinions, findings, and conclusions or recommendations expressed in this material are those of the author(s) and do not necessarily reflect the views of CRESCENT or its sponsors. The research is also supported by NASA award #80NSSC23K1326.

Data and code availability

Hydrodynamic modeling was carried out with the GeoClaw module of Clawpack v5.11, an open source code for solving the tsunami shallow water equations archived in Zenodo (Clawpack Development Team, 2024). The stochastic source used in Figure 10 was generated using FakeQuakes, a module of MudPy open source stochastic rupture generator archived on Zenodo at Melgar et al. (2021). Ruptures used as input and hydrodynamic model output are also archived on Zenodo at Melgar (2025).

Competing interests

The author declares no competing interests.

References

Allen, T. I. and Hayes, G. P. Alternative Rupture-Scaling Relationships for Subduction Interface and Other Offshore Environ-

ments. *Bulletin of the Seismological Society of America*, 107(3): 1240–1253, Mar. 2017. doi: 10.1785/0120160255.

Arcos, M. E. M. and LeVeque, R. J. Validating Velocities in the GeoClaw Tsunami Model Using Observations near Hawaii from the 2011 Tohoku Tsunami. *Pure and Applied Geophysics*, 172(3–4): 849–867, Nov. 2014. doi: 10.1007/s00024-014-0980-y.

Baba, T., Allgeyer, S., Hossen, J., Cummins, P. R., Tsushima, H., Imai, K., Yamashita, K., and Kato, T. Accurate numerical simulation of the far-field tsunami caused by the 2011 Tohoku earthquake, including the effects of Boussinesq dispersion, seawater density stratification, elastic loading, and gravitational potential change. *Ocean Modelling*, 111:46–54, Mar. 2017. doi: 10.1016/j.ocemod.2017.01.002.

Becker, J. J., Sandwell, D. T., Smith, W. H. F., Braud, J., Binder, B., Depner, J., Fabre, D., Factor, J., Ingalls, S., Kim, S.-H., Ladner, R., Marks, K., Nelson, S., Pharaoh, A., Trimmer, R., Von Rosenberg, J., Wallace, G., and Weatherall, P. Global Bathymetry and Elevation Data at 30 Arc Seconds Resolution: SRTM30_PLUS. *Marine Geodesy*, 32(4):355–371, Nov. 2009. doi: 10.1080/01490410903297766.

Berger, M. J., George, D. L., LeVeque, R. J., and Mandli, K. T. The GeoClaw software for depth-averaged flows with adaptive refinement. *Advances in Water Resources*, 34(9):1195–1206, Sept. 2011. doi: 10.1016/j.advwatres.2011.02.016.

Bilek, S. L. and Lay, T. Rigidity variations with depth along interplate megathrust faults in subduction zones. *Nature*, 400(6743): 443–446, July 1999. doi: 10.1038/22739.

Blaser, L., Kruger, F., Ohrnberger, M., and Scherbaum, F. Scaling Relations of Earthquake Source Parameter Estimates with Special Focus on Subduction Environment. *Bulletin of the Seismological Society of America*, 100(6):2914–2926, Dec. 2010. doi: 10.1785/0120100111.

Butler, R., Walsh, D., and Richards, K. Extreme tsunami inundation in Hawai'i from Aleutian–Alaska subduction zone earthquakes. *Natural Hazards*, 85(3):1591–1619, Nov. 2016. doi: 10.1007/s11069-016-2650-0.

Clawpack Development Team. Clawpack v5.11.0, Aug. 2024. doi: 10.5281/zenodo.13376470.

Crowell, B. W. and Melgar, D. Slipping the Shumagin Gap: A Kinematic Coseismic and Early Afterslip Model of the Mw 7.8 Simeonof Island, Alaska, Earthquake. *Geophysical Research Letters*, 47(19), Oct. 2020. doi: 10.1029/2020gl090308.

Davies, G. and Griffin, J. *The 2018 Australian probabilistic tsunami hazard assessment: hazard from earthquake generated tsunamis*. Geoscience Australia, 2018. doi: 10.11636/record.2018.041.

Davies, G., Horspool, N., and Miller, V. Tsunami inundation from heterogeneous earthquake slip distributions: Evaluation of synthetic source models. *Journal of Geophysical Research: Solid Earth*, 120(9):6431–6451, Sept. 2015. doi: 10.1002/2015jb012272.

Fujii, Y. and Satake, K. Tsunami Source of the 2004 Sumatra–Andaman Earthquake Inferred from Tide Gauge and Satellite Data. *Bulletin of the Seismological Society of America*, 97(1A): S192–S207, Jan. 2007. doi: 10.1785/0120050613.

Geist, E. and Lynett, P. Source Processes for the Probabilistic Assessment of Tsunami Hazards. *Oceanography*, 27(2):86–93, June 2014. doi: 10.5670/oceanog.2014.43.

Geist, E. L. Complex earthquake rupture and local tsunamis. *Journal of Geophysical Research: Solid Earth*, 107(B5), May 2002. doi: 10.1029/2000jb000139.

Geist, E. L. and Parsons, T. Probabilistic Analysis of Tsunami Hazards*. *Natural Hazards*, 37(3):277–314, Mar. 2006. doi: 10.1007/s11069-005-4646-z.

Glimsdal, S., Pedersen, G. K., Harbitz, C. B., and Løvholt, F. Dispersion of tsunamis: does it really matter? *Natural Hazards and Earth System Sciences*, 13(6):1507–1526, June 2013. doi: 10.5194/nhess-13-1507-2013.

Goda, K., Mai, P. M., Yasuda, T., and Mori, N. Sensitivity of tsunami wave profiles and inundation simulations to earthquake slip and fault geometry for the 2011 Tohoku earthquake. *Earth, Planets and Space*, 66(1), Sept. 2014. doi: 10.1186/1880-5981-66-105.

González, F. I., Geist, E. L., Jaffe, B., Kânoğlu, U., Mofjeld, H., Synolakis, C. E., Titov, V. V., Arcas, D., Bellomo, D., Carlton, D., Horning, T., Johnson, J., Newman, J., Parsons, T., Peters, R., Peterson, C., Priest, G., Venturato, A., Weber, J., Wong, F., and Yalciner, A. Probabilistic tsunami hazard assessment at Seaside, Oregon, for near- and far-field seismic sources. *Journal of Geophysical Research: Oceans*, 114(C11), Nov. 2009. doi: 10.1029/2008jc005132.

González, F. I., LeVeque, R. J., Chamberlain, P., Hirai, B., Varkovitzky, J., and George, D. L. Validation of the GeoClaw model. In *NTHMP MMS tsunami inundation model validation workshop*, pages 1–84. GeoClaw Tsunami Modeling Group University of Washington, 2011. https://depts.washington.edu/clawpack/links/nthmp-benchmarks/geoclaw-results.pdf.

González, J., González, G., Aránguiz, R., Melgar, D., Zamora, N., Shrivastava, M. N., Das, R., Catalán, P. A., and Cienfuegos, R. A hybrid deterministic and stochastic approach for tsunami hazard assessment in Iquique, Chile. *Natural Hazards*, 100(1): 231–254, Oct. 2019. doi: 10.1007/s11069-019-03809-8.

Grezio, A., Babeyko, A., Baptista, M. A., Behrens, J., Costa, A., Davies, G., Geist, E. L., Glimsdal, S., González, F. I., Griffin, J., Harbitz, C. B., LeVeque, R. J., Lorito, S., Løvholt, F., Omira, R., Mueller, C., Paris, R., Parsons, T., Polet, J., Power, W., Selva, J., Sørensen, M. B., and Thio, H. K. Probabilistic Tsunami Hazard Analysis: Multiple Sources and Global Applications. *Reviews of Geophysics*, 55(4):1158–1198, Dec. 2017. doi: 10.1002/2017rg000579.

Grilli, S. T., Harris, J. C., Tajalli Bakhsh, T. S., Masterlark, T. L., Kyriakopoulos, C., Kirby, J. T., and Shi, F. Numerical Simulation of the 2011 Tohoku Tsunami Based on a New Transient FEM Coseismic Source: Comparison to Far- and Near-Field Observations. *Pure and Applied Geophysics*, 170(6–8):1333–1359, July 2012. doi: 10.1007/s00024-012-0528-y.

Hayes, G. P., Moore, G. L., Portner, D. E., Hearne, M., Flamme, H., Furtney, M., and Smoczyk, G. M. Slab2, a comprehensive subduction zone geometry model. *Science*, 362(6410):58–61, Oct. 2018. doi: 10.1126/science.aat4723.

Hill, E. M., Borrero, J. C., Huang, Z., Qiu, Q., Banerjee, P., Natawidjaja, D. H., Elosegui, P., Fritz, H. M., Suwargadi, B. W., Pranantyo, I. R., Li, L., Macpherson, K. A., Skanavis, V., Synolakis, C. E., and Sieh, K. The 2010 Mw 7.8 Mentawai earthquake: Very shallow source of a rare tsunami earthquake determined from tsunami field survey and near-field GPS data. *Journal of Geophysical Research: Solid Earth*, 117(B6), June 2012. doi: 10.1029/2012jb009159.

Hirshorn, B., Weinstein, S., Wang, D., Koyanagi, K., Becker, N., and McCreery, C. *Earthquake Source Parameters, Rapid Estimates for Tsunami Forecasts and Warnings*, pages 1–35. Springer Berlin Heidelberg, Berlin, Heidelberg, 2020. doi: 10.1007/978-3-642-27737-5_160-2.

Horspool, N., Pranantyo, I., Griffin, J., Latief, H., Natawidjaja, D. H., Kongko, W., Cipta, A., Bustaman, B., Anugrah, S. D., and Thio, H. K. A probabilistic tsunami hazard assessment for Indonesia. *Natural Hazards and Earth System Sciences*, 14(11):3105–3122,

2014. doi: 10.5194/nhess-14-3105-2014.

Ichinose, G., Somerville, P., Thio, H. K., Graves, R., and O'Connell, D. Rupture process of the 1964 Prince William Sound, Alaska, earthquake from the combined inversion of seismic, tsunami, and geodetic data. *Journal of Geophysical Research: Solid Earth*, 112(B7), July 2007. doi: 10.1029/2006jb004728.

Kanamori, H. Mechanism of tsunami earthquakes. *Physics of the Earth and Planetary Interiors*, 6(5):346–359, Jan. 1972. doi: 10.1016/0031-9201(72)90058-1.

LeVeque, R. J., George, D. L., and Berger, M. J. Tsunami modelling with adaptively refined finite volume methods. *Acta Numerica*, 20:211–289, Apr. 2011. doi: 10.1017/s0962492911000043.

Li, L., Switzer, A. D., Chan, C., Wang, Y., Weiss, R., and Qiu, Q. How heterogeneous coseismic slip affects regional probabilistic tsunami hazard assessment: A case study in the South China Sea. *Journal of Geophysical Research: Solid Earth*, 121(8): 6250–6272, Aug. 2016. doi: 10.1002/2016jb013111.

Mandli, K. T., Ahmadia, A. J., Berger, M., Calhoun, D., George, D. L., Hadjimichael, Y., Ketcheson, D. I., Lemoine, G. I., and LeVeque, R. J. Clawpack: building an open source ecosystem for solving hyperbolic PDEs. *PeerJ Computer Science*, 2:e68, Aug. 2016. doi: 10.7717/peerj-cs.68.

Melgar, D. Model output data for Alaska far-field tsunami simulations, Mar. 2025. doi: 10.5281/zenodo.15085678.

Melgar, D. and Bock, Y. Kinematic earthquake source inversion and tsunami runup prediction with regional geophysical data. *Journal of Geophysical Research: Solid Earth*, 120(5):3324–3349, May 2015. doi: 10.1002/2014jb011832.

Melgar, D. and Hayes, G. P. Systematic Observations of the Slip Pulse Properties of Large Earthquake Ruptures. *Geophysical Research Letters*, 44(19):9691–9698, Oct. 2017. doi: 10.1002/2017gl074916.

Melgar, D., Williamson, A. L., and Salazar-Monroy, E. F. Differences between heterogenous and homogenous slip in regional tsunami hazards modelling. *Geophysical Journal International*, 219(1):553–562, July 2019. doi: 10.1093/gji/ggz299.

Melgar, D., Lin, T., Kong, Q., christineruhl, and Marfito, B. dmelgar-m/MudPy: v1.3, Sept. 2021. doi: 10.5281/zenodo.5397091.

Mori, N., Takahashi, T., Yasuda, T., and Yanagisawa, H. Survey of 2011 Tohoku earthquake tsunami inundation and runup. *Geophysical Research Letters*, 38(7), Apr. 2011. doi: 10.1029/2011gl049210.

Mori, N., Goda, K., and Cox, D. *Recent Process in Probabilistic Tsunami Hazard Analysis (PTHA) for Mega Thrust Subduction Earthquakes*, page 469–485. Springer International Publishing, July 2017. doi: 10.1007/978-3-319-58691-5_27.

Newman, A. V. and Okal, E. A. Teleseismic estimates of radiated seismic energy: The E/M0 discriminant for tsunami earthquakes. *Journal of Geophysical Research: Solid Earth*, 103(B11): 26885–26898, Nov. 1998. doi: 10.1029/98jb02236.

NOAA National Geophysical Data Center. 2-minute gridded global relief data (ETOPO2) v2. *NOAA National Centers for Environmental Information*, 2006. doi: 10.7289/V5J1012Q.

Nosov, M. A., Bolshakova, A. V., and Kolesov, S. V. Displaced Water Volume, Potential Energy of Initial Elevation, and Tsunami Intensity: Analysis of Recent Tsunami Events. *Pure and Applied Geophysics*, 171(12):3515–3525, Nov. 2013. doi: 10.1007/s00024-013-0730-6.

Okada, Y. Surface deformation due to shear and tensile faults in a half-space. *Bulletin of the Seismological Society of America*, 75 (4):1135–1154, Aug. 1985. doi: 10.1785/bssa0750041135.

Okada, Y. Internal deformation due to shear and tensile faults in a half-space. *Bulletin of the Seismological Society of America*, 82 (2):1018–1040, Apr. 1992. doi: 10.1785/bssa0820021018.

Powers, P. M., Altekruse, J. M., Llenos, A. L., Michael, A. J., Haynie, K. L., Haeussler, P. J., Bender, A. M., Rezaeian, S., Moschetti, M. P., Smith, J. A., Briggs, R. W., Witter, R. C., Mueller, C. S., Zeng, Y., Girot, D. L., Herrick, J. A., Shumway, A. M., and Petersen, M. D. The 2023 Alaska National Seismic Hazard Model. *Earthquake Spectra*, 40(4):2545–2597, Aug. 2024. doi: 10.1177/87552930241266741.

Priest, G. R., Witter, R. C., Zhang, Y. J., Wang, K., Goldfinger, C., Stimely, L. L., English, J. T., Pickner, S. G., Hughes, K. L., Wille, T. E., et al. Tsunami inundation scenarios for Oregon. *Oregon Department of Geology Mineral Industries Open-File Report O-13*, 19, 2013. https://d3itl75cn7661p.cloudfront.net/dogami/ofr/O-19-04_report.pdf.

Riquelme, S. and Fuentes, M. Tsunami Efficiency Due to Very Slow Earthquakes. *Seismological Research Letters*, 92(5):2998–3006, Apr. 2021. doi: 10.1785/0220200198.

Riquelme, S., Schwarze, H., Fuentes, M., and Campos, J. Near-Field Effects of Earthquake Rupture Velocity Into Tsunami Runup Heights. *Journal of Geophysical Research: Solid Earth*, 125(6), June 2020. doi: 10.1029/2019jb018946.

Ruiz-Angulo, A., Melgar, D., de Marez, C., Deniau, A., Nencioli, F., and Hjörleifsdóttir, V. SWOT Satellite Altimetry Observations and Source Model for the Tsunami from the 2025 M8.8 Kamchatka Earthquake. *The Seismic Record*, 5(4):341–351, Oct. 2025. doi: 10.1785/0320250037.

Sahakian, V., Melgar, D., and Muzli, M. Weak Near-Field Behavior of a Tsunami Earthquake: Toward Real-Time Identification for Local Warning. *Geophysical Research Letters*, 46(16):9519–9528, Aug. 2019. doi: 10.1029/2019gl083989.

Saito, T. and Furumura, T. Three-dimensional tsunami generation simulation due to sea-bottom deformation and its interpretation based on the linear theory. *Geophysical Journal International*, 178(2):877–888, Aug. 2009. doi: 10.1111/j.1365-246x.2009.04206.x.

Salazar-Monroy, E. F., Melgar, D., Jaimes, M. A., and Ramirez-Guzman, L. Regional Probabilistic Tsunami Hazard Analysis for the Mexican Subduction Zone From Stochastic Slip Models. *Journal of Geophysical Research: Solid Earth*, 126(6), June 2021. doi: 10.1029/2020jb020781.

Sementsov, K. A., Baba, T., Kolesov, S. V., Tanioka, Y., and Nosov, M. A. The effect of earthquake fault rupture kinematics on tsunami generation: a numerical study of real events. *Geophysical Journal International*, 240(2):920–941, Nov. 2024. doi: 10.1093/gji/ggae413.

Sepúlveda, I., Liu, P. L., and Grigoriu, M. Probabilistic Tsunami Hazard Assessment in South China Sea With Consideration of Uncertain Earthquake Characteristics. *Journal of Geophysical Research: Solid Earth*, 124(1):658–688, Jan. 2019. doi: 10.1029/2018jb016620.

Suppasri, A., Imamura, F., and Koshimura, S. Effects of the Rupture Velocity of Fault Motion, Ocean Current and Initial Sea Level on the Transoceanic Propagation of Tsunami. *Coastal Engineering Journal*, 52(2):107–132, June 2010. doi: 10.1142/s0578563410002142.

Sørensen, M. B., Spada, M., Babeyko, A., Wiemer, S., and Grünthal, G. Probabilistic tsunami hazard in the Mediterranean Sea. *Journal of Geophysical Research: Solid Earth*, 117(B1), Jan. 2012. doi: 10.1029/2010jb008169.

Taha, B. A., Addie, A. J., Haider, A. J., Osman, S. A., Ramli, M. Z., and Arsad, N. A review of seismic detection using fiber optic distributed acoustic sensing: from telecommunication cables to earthquake sensors. *Natural Hazards*, 121(12):13927–13959, May 2025. doi: 10.1007/s11069-025-07370-5.

Tanioka, Y. and Satake, K. Tsunami generation by horizontal displacement of ocean bottom. *Geophysical Research Letters*, 23 (8):861–864, Apr. 1996. doi: 10.1029/96gl00736.

Titov, V., Rabinovich, A. B., Mofjeld, H. O., Thomson, R. E., and González, F. I. The Global Reach of the 26 December 2004 Sumatra Tsunami. *Science*, 309(5743):2045–2048, Sept. 2005. doi: 10.1126/science.1114576.

UNDRR, C. *Economic losses, poverty & disasters: 1998-2017*. United Nations Office for Disaster Risk Reduction, 2018. https://www.undrr.org/publication/economic-losses-poverty-disasters-1998-2017.

University of Washington Working Group. *Probabilistic Tsunami Design Maps for the ASCE 7-16 Standard*, page 1–17. American Society of Civil Engineers, June 2017. doi: 10.1061/9780784480748.001.

Williamson, A., Melgar, D., and Rim, D. The Effect of Earthquake Kinematics on Tsunami Propagation. *Journal of Geophysical Research: Solid Earth*, 124(11):11639–11650, Nov. 2019. doi: 10.1029/2019jb017522.

Wilson, A. and Ma, S. Wedge Plasticity and Fully Coupled Simulations of Dynamic Rupture and Tsunami in the Cascadia Subduction Zone. *Journal of Geophysical Research: Solid Earth*, 126(7), July 2021. doi: 10.1029/2020jb021627.

Witter, R. C., Zhang, Y., Wang, K., Priest, G. R., Goldfinger, C., Stimely, L. L., English, J. T., and Ferro, P. A. Simulating tsunami inundation at Bandon, Coos County, Oregon, using hypothetical Cascadia and Alaska earthquake scenarios. *Oregon Department of Geology and Mineral Industries Special Paper 43*, page 57, 2011. https://digitalcollections.library.oregon.gov/nodes/view/162548.

Ye, L., Bai, Y., Si, D., Lay, T., Cheung, K. F., and Kanamori, H. Rupture Model for the 29 July 2021 MW 8.2 Chignik, Alaska Earthquake Constrained by Seismic, Geodetic, and Tsunami Observations. *Journal of Geophysical Research: Solid Earth*, 127(7), July 2022. doi: 10.1029/2021jb023676.